Degradation Mechanisms and Partial Shading of Glass-backsheet and Double-glass Photovoltaic Modules in Three Climate Zones Determined by Remote Monitoring of Time-series Current-voltage and Power Datastreams

Jiqi Liu[a,b,1], Menghong Wang[a,c], Alan J. Curran[a,b], Erdmut Schnabel[e], Michael Köhl[e], Jennifer L. Braid[a,b,f], Roger H. French[a,b,c,d,1,*]

[a]*SDLE Research Center, Case Western Reserve University, Cleveland OH, 44106, USA*
[b]*Materials Science Department, Case Western Reserve University, Cleveland OH, 44106, USA*
[c]*Macromolecular Science Department, Case Western Reserve University, Cleveland OH, 44106, USA*
[d]*Computer & Data Sciences Department, Case Western Reserve University, Cleveland OH, 44106, USA*
[e]*Fraunhofer Institute for Solar Energy Systems (ISE), Heidenhofstrasse 2, 79110 Freiburg, Germany*
[f]*Sandia National Laboratories, Albuquerque NM, 87123, USA*

Abstract

Degradation and partial shading impact the long-term reliability and power production of photovoltaic (PV) modules and power plants. Time-series power (P_{mp}) and current-voltage (I-V) curve datastreams from PV modules enable a remote diagnostic approach to quantify active degradation mechanisms and identify partial shading. We study three to nine years of these datastreams, including 3.6 million I-V curves and 36 million P_{mp} values, from eight PV modules, four each of double-glass and glass-backsheet module architectures, located in three distinctly different Köppen-Geiger climate zones, to determine the module's performance loss rates (PLR), identify active degradation mechanisms and power loss modes, along with partial shading by local objects. Considering both module architectures, PLR results indicate that the BSh climate

*Roger H. French
Email address: roger.french@case.edu (Roger H. French)
[1]ISES member

zone is the most aggressive for module degradation, while the Alpine ET zone is the mildest climate. PLR of double-glass modules located in BWh and BSh climate zones are different due to the significantly greater uniform current loss (ΔP_{Isc}) for double-glass modules in BSh, at a 5% significance level. Power loss for four out of five modules located in the BWh and BSh climates are dominated by uniform current degradation. Statistical analysis of multistep I-V curves detects partial shading experienced by three studied modules with details of the shading profile, the shading Poynting vector diagram for the obstacle's relative position, shading scenarios, and duration. This work demonstrates how remote monitoring and diagnosis of P_{mp} & I-V time-series of modules can provide quantitative operations and maintenance insights into system performance, degradation mechanisms, and shading.

Keywords: Degradation, Partial shading, P_{mp} & I-V time-series, outdoor I_{sc}-V_{oc}, Remote Monitoring

1. Introduction

Due to the rapid growth of solar energy (Cozzi et al. (2020); Perea et al. (2019)) and the development of low-cost I-V tracing equipment (Jones et al. (2018); Jones & Hansen (2019); Pordis (2018)) in the past few years, detailed time-series electrical data has become increasingly accessible, providing opportunities to remotely study the behavior of PV modules installed in the field. The two most common types of time-series electrical data, maximum power (P_{mp}) and current-voltage (I-V) curves, can be used to evaluate degradation behavior (Jordan et al. (2010); Smith et al. (2012); French et al. (2015); Peshek et al. (2016)) and detect the operational status of PV modules (Nehme et al. (2017)). Time-series P_{mp} data can be utilized to calculate the performance loss rate (PLR) (Curran et al. (2019, 2020)). There are multiple methods developed for calculating PLR, and these procedures contain four steps (Lindig et al. (2021); French et al. (2021); Lindig et al. (2018); Davis et al. (2013); Marion et al. (2005)), beginning with data cleaning and filtering, then choosing a

performance metric such as performance ratio (Phinikarides et al. (2014)), predicted power (Curran et al. (2019)), PVUSA (Whitaker et al. (1997)), or Sandia PV Array Performance Model (Kratochvil et al. (2004)). Then time-series regression methods are applied, such as the seasonal and trend decomposition (Jordan & Kurtz (2010)), and linear or *year-on-year* (Jordan et al. (2018)) regression to determine the PLR of PV systems.

In contrast with P_{mp} which indicates the overall performance of a PV module or system, I-V curves are able to provide more insight into PV module degradation modes and mechanisms (Liu et al. (2019)) with suitable analysis methods. The outdoor I_{sc}-V_{oc} curve can be used to obtain more degradation information especially when comparing with features extracted from the I-V curve under the same conditions (Siyu Guo et al. (2016); Killam et al. (2021)). The outdoor I_{sc}-V_{oc} and power loss factor method developed by M. Wang (Wang et al. (2021); Gok et al. (2021)) can convert the change in I-V features into power loss factors, enabling direct comparisons and rank ordering of activated degradation modes. Studies of long-term PV module degradation guide development of modules and systems with longer lifetimes to reduce the levelized cost of PV energy.

Power degradation and faults, if not detected, can not only cause power loss, but also threaten the security, safety, and reliability of the whole PV power plant (Nehme et al. (2017)). During partial shading events, nearby objects cast shadows onto part of a PV module or array, causing spatially non-uniform irradiance (Meyers & Mikofski (2017)). This partial shading causes power loss, as seen with uniform shading, but also induces changes in the module degradation due to frequent bypass diode activation, reverse biasing of cells, and the subsequent generation of local hot spots. These effects can cause overheating and severe, non-uniform degradation of the module packaging materials (Basri et al. (2015)), particularly in cases where an object repeatedly shades the module or array (e.g., at the same time every day). Shading detection methods, using time-series P_{mp}, are quite mature (Tsafarakis et al. (2019)), but they can't distinguish between partial and uniform shading cases and most of these

methods require an unshaded reference system such as a nearby pyranometer that is guaranteed not to experience shading (Tsafarakis et al. (2019); Firth et al. (2009)). Partial shading in most cases will cause distortion, or a "step", in the I-V curve, which is not observed in the uniform shading case (Basri et al. (2015)). This distinction provides an opportunity to detect partial shading without a reference system. Current studies using I-V curves for shading detection focus on the relationship between different shading geometries and the corresponding shapes of the I-V curves (Basri et al. (2015); Hemza et al. (2019); Teodorescu et al. (2015)), but they lack methods to analyze time-series I-V curves so as to detect partial shading conditions for modules in the field.

In this paper, we obtained the performance loss rate (PLR) and the rates of four power loss modes of eight PV modules located in three climate zones. We determined the dependence of degradation behavior on the PV modules' architectures, manufacturers, and the climate zones where they were exposed, and identified dominant degradation modes for each. In addition, a statistical analysis using time-series I-V curves for partial shading detection was developed to provide a module's shading scenario and duration, its temporal partial shading profile, and the shading Poynting vector of shading obstacles' relative position.

2. Dataset Description

The P_{mp}, I-V time-series datasets were acquired by Fraunhofer-ISE from their outdoor test facilities. The dataset contains time-series P_{mp} recorded every minute and I-V curves recorded every five minutes by the I-V tracing equipment (ET Instrumente GmbH), module temperature measured every minute for each module, and global irradiance in the plane of array (POA) for every minute. Each I-V curve contains 40 to 70 points, and the I-V tracer also records the I-V features it extracts, including maximum power (P_{mp}), voltage at maximum power (V_{mp}), current at maximum power (I_{mp}), short-circuit current (I_{sc}), open-circuit voltage (V_{oc}), series resistance (R_s), shunt resistance (R_{sh}), and fill factor

(FF).

The eight PV modules studied (Table 1) are located in three distinct Köppen-Geiger climatic zones (Rubel et al. (2017)) and belong to two brands. The climate zones are identified by their longitude and latitude using the *kgc* R package (Bryant et al. (2017); R Core Team (2020)). The Köppen-Geiger climate classification divides climates into five main climate "groups" indicated by the first letter, where for example B is arid and E is polar. These main climate groups range from A for the tropical climates near the equator to E at the north or south pole. The second letter indicates the seasonal precipitation "type", where W is for desert, S is for steppe, and T is for tundra. If the annual precipitation is less than 50% of a threshold, which is determined by the seasonal percentage of precipitation and the average annual temperature, the climate is classified as BW, otherwise, the classification is BS. So BSh has more precipitation than BWh, but both have less precipitation than any of the A tropical climates. The third letter is the temperature "subtype" and indicates the level of heat in the climate zone, where h is for hot indicating the average annual temperature above 18 °C. ET is much colder than both BWh and BSh, and it only has an average temperature below 10°C for every month. The brand F module is a glass-backsheet (GB) module with a polymeric backsheet, while the brand G module has a double-glass (DG) module architecture.

Table 1: Information on the PV modules studied: their exposure start and end dates, installation locations, brand:module architectures, and numbers of cells and bypass diodes.

ID	Start	End	System Age (Year)	Climate Zone	Latitude (°)	Longitude (°)	Brand	# of Cells	# of Bypass Diodes
1	2010-10-19	2018-10-31	8.03	BWh	27.82	-15.42	G:DG	80	4
2	2010-02-05	2018-10-31	8.74	BWh	27.82	-15.42	G:DG	72	3
3	2010-09-28	2016-11-24	6.16	BWh	27.82	-15.42	F:GB	60	3
4	2012-06-11	2018-10-31	6.39	BSh	30.86	34.78	G:DG	80	4
5	2012-06-11	2015-05-17	2.93	BSh	30.86	34.78	F:GB	60	3
6	2012-06-11	2018-10-31	6.39	BSh	30.86	34.78	F:GB	60	3
7	2010-06-16	2013-01-31	2.63	ET	47.42	10.89	G:DG	80	4
8	2010-06-16	2015-02-18	4.69	ET	47.42	10.89	F:GB	60	3

3. Analytical Methods

In this section, we introduce several analytical methods used to evaluate our dataset, including the XbX with universal temperature correction (XbX+UTC) method (Curran et al. (2019)) and the *year-on-year* method (Hasselbrink et al. (2013); Jordan et al. (2018)) to obtain the performance loss rate (PLR) (French et al. (2021)), outdoor I_{sc}-V_{oc} and power loss factor method (Wang et al. (2020)) with *month-by-month* regression to determine the rate of change of each power loss mode, I-V curves quality detection and the partial shading detection method. The XbX+UTC and outdoor I_{sc}-V_{oc} methods are already published as open-source R code packages (R Core Team (2020)) available on CRAN as $Suns$-V_{oc} and $PVplr$ respectively (Wang et al. (2021); Curran et al. (2020)). The partial shading detection method uses our data-driven I-V feature extraction R package (*ddiv*) to detect steps in the I-V curves (Huang et al. (2021)). In addition, our outdoor I_{sc}-V_{oc} results use the tracer-reported I-V features, including I_{sc}, V_{oc}, I_{mp}, V_{mp} and R_s. When I-V features are not reported by the tracer, *ddiv* is the suggested method to extract the I-V features for outdoor I_{sc}-V_{oc} analysis.

3.1. Performance Loss Rate (PLR) Calculation

Time-series P_{mp}, POA, and module temperature are used as inputs to determine PLR. The $XbX+UTC$ analysis has four steps and provides the predicted P_{mp} at a given reference condition for each X time period, which can be a day, week, month or any other time period (Curran et al. (2019)). In this study we choose X as one day and the reference condition chosen is POA of 900 W/m^2 and module temperature of 40 °C. First, a low irradiance cutoff of 200 W/m^2 is applied to filter the P_{mp} data. Second, a temperature coefficient is obtained, using a linear model of P_{mp} versus module temperature, for irradiances of 900 ± 10 W/m^2. Third, a temperature correction is applied to correct each P_{mp} value to the reference temperature. Finally, a linear model of temperature corrected P_{mp} versus POA is fit using observations of each day, and the daily predicted

P_{mp} result at the reference POA is obtained. This daily predicted P_{mp} is then analyzed using *year-on-year* regression (Hasselbrink et al. (2013); Jordan et al. (2018)) to obtain a PLR distribution of each module.

3.2. Outdoor I_{sc}-V_{oc} and Power Loss Factor Calculation

The outdoor I_{sc}-V_{oc} and power loss factor method proposed by M. Wang (Wang et al. (2020)) requires time-series I-V features including I_{sc}, V_{oc}, I_{mp}, V_{mp},R_s, and POA, and module temperature, and the resulting output is the four kinds of power loss modes in each time period (typically one week for our study) at 1 Sun POA irradiance and the reference module temperature, which is 40 °C in this study. The four power loss modes correspond to uniform current loss (ΔP_{Isc}), recombination (ΔP_{Voc}), series resistance (ΔP_{Rs}) and current mismatch (ΔP_{Imis}). In our study, these weekly time-series power losses are normalized by the initial predicted P_{mp} at the same reference condition, which is obtained by a linear model fit using the weekly predicted P_{mp} from the outdoor I_{sc}-V_{oc} method at the defined reference condition. Then these normalized power losses are grouped into months to get an estimated rate of change for each power loss mode using the *month-by-month* regression method, which provides twelve slopes obtained from the linear model using monthly data across years.

3.3. Quality Detection of Current-voltage curves

It's very important to remove the anomalous or non-physical I-V curves from the input dataset prior to further analysis, such as for step detection. We therefore have developed an I-V quality detection algorithm that evaluates I-V curves based on physical constraints using two user-determined hyperparameters, P_1 and P_2. To be physically reasonable, considering a single diode model, the first derivative $\frac{\partial I}{\partial V}$ must be negative, which indicates that datapoints with increasing voltage should have decreasing current (Gow & Manning (1999)). However, I-V tracing instruments have finite measurement accuracy, which we use to determine the value of P_1. We first sort the datapoints of the I-V curve in increasing voltage order, then calculate the current difference by I_i - I_{i-1}. If

this difference is larger than P_1, we define point i as an unqualified data point. If the number of unqualified data points is larger than the value of P_2 we have set, the curve is labeled as unqualified and not used in further analysis. In our study, P_1 is set to 0.02 A based on the instrument specification, and P_2 is set to zero. The non-physical or unqualified curves are removed only for the partial shading analysis. The P_2 hyperparameter can be increased to tolerate more noise in I-V curves and reduce the number of curves that are filtered.

3.4. Partial Shading Detection

The *ddiv* algorithm also has two user-determined hyperparameters for detecting steps in I-V curves: the maximum number of change points (k) and the critical value of the slope difference before and after the step (m^a_Δ) (Huang et al. (2021)). The *ddiv* algorithm returns the total number of steps, the voltage position of each detected step, and the I-V features of each step. Fig. 1 shows examples of single step and multistep I-V curves with the middle steps' location (steps except the last one located at V_{oc}) obtained from *ddiv* using the package default hyperparameter settings.

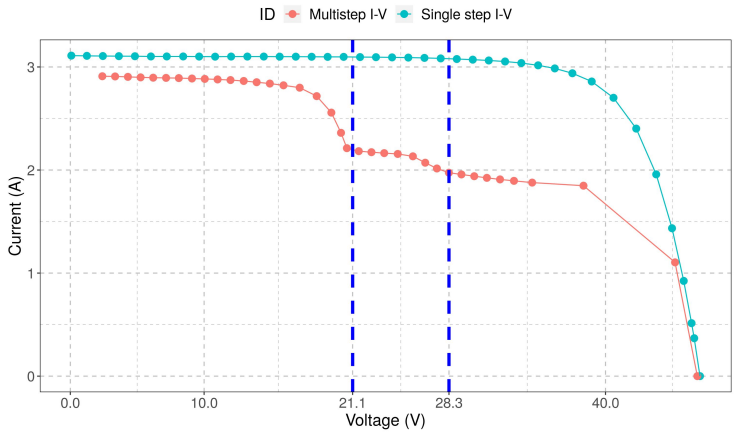

Figure 1: Single step and multistep I-V curves with detected middle steps' location in volts.

A randomly chosen and manually labeled dataset is required for determining the hyperparameters k and m^a_Δ. We randomly selected ten thousands I-V

curves from the entire dataset (including all modules) and manually labeled them as single step or multistep I-V curves. Then one thousand single step and one thousand multistep I-V curves were randomly selected from these ten thousand labeled curves. We divided each group of I-V curves into training and testing datasets with 80%/20% partitioning. A grid search was performed to determine the optimal hyperparameters k and m_{Δ}^{a} for the training dataset. The testing dataset was used to verify that the optimal hyperparameters did not overfit the training dataset. k is the number of change points allowed in an I-V curve, which should be at least large enough to support all physically possible cases, determined by the number of bypass diodes installed in the PV module (there are typically 2 change points associated with each step in the I-V curve). These two hyperparameters were determined considering both the overall step detection accuracy, and the balance between identifying single step and multistep I-V curves. The overall accuracy obtained from the training dataset is also used to determine whether a module has experienced partial shading: PV modules with a percentage of multistep I-V curves (MS) higher than the model accuracy are confirmed to experience partial shading, and these data are further processed to obtain details of shading conditions.

First, we study the time dependence of the multistep I-V curves to obtain a shading profile indicating what times of the day or year partial shading occurs. For each year, the MS of each daily time point is calculated, then a local peak finding function "findpeak" from the *pracma* R package (Borchers (2019)) is applied to find the local peak of the MS in time. Next, we study the shading Poynting vector diagram of the occurrence of multistep I-V curves, with axes of the solar azimuth and elevation angles, to determine the relative orientation of shading obstacles to the module. Using the "getSunlightPosition" function in the *suncalc* R package (Thieurmel & Elmarhraoui (2019)), we obtain the elevation and azimuth angles from the date, time, and module location. We calculate the MS in one-degree intervals of the azimuth angle, then find the localized peak locations, which represent the relative orientation of shading obstacles to the module under study. Then we study the shading scenarios

using the I-V step voltages in the multistep I-V curves. Previous research shows that the step voltages in the I-V curve correspond to different shading scenarios, and we can use this to classify the multistep I-V curves into three cases for a PV module with three bypass diodes (Basri et al. (2015)). The three cases (all for modules containing 3 strings of PV cells) are: one bypass diode activated as indicated by one step located close to V_{oc}, two bypass diodes activated with similar current mismatch indicated by one step located closer to 0 V, and two bypass diodes activated with different current mismatch indicated by two steps between 0 V and V_{oc} (Basri et al. (2015)). Finally, the percentage of each partial shading case, and the duration of partial shading from the number of consecutive multistep I-V curves are also obtained.

Fig. 2 is a flowchart for applying partial shading detection to a module's time-series I-V data. The blue box is for the data input, while green boxes are for the outputs. As mentioned before, if the I-V tracer does not report all features needed for outdoor I_{sc}-V_{oc} analysis (or these reported features are inaccurate), then outdoor I_{sc}-V_{oc} analysis and partial shading detection could share processing steps including the quality detection of I-V curves and *ddiv* for feature extraction.

4. Results

4.1. Long Term Performance and Degradation of PV Modules

Fig. 3 shows the median and 83.4% confidence interval (CI) of the PLR for each module, colored by climate zones and with different point shapes for the module architectures (brands). We use 83.4% CIs to infer a p-value close to 0.05 (a 5% significance level) when the CI boundaries of two samples touch (Cumming & Finch (2005)). Fig. 4 shows the four normalized power loss factors for module 2 (BWh climate zone: DG module architecture) obtained from outdoor I_{sc}-V_{oc} analysis, with fitted linear models. For each module, we remove the outliers of each power loss mode with Tukey outlier parameter γ as

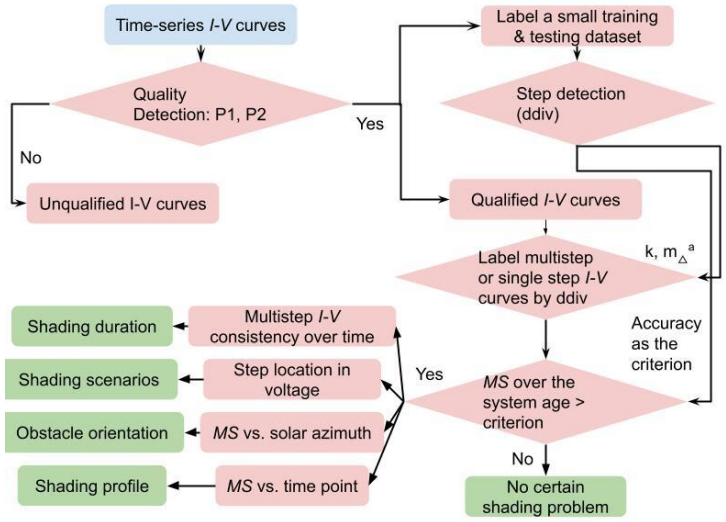

Figure 2: A flowchart of the partial shading detection analysis method applied to one PV module.

1.5 using Eq. 1, in which Q_1 and Q_3 are the lower and upper quartiles (Tukey (1977)).

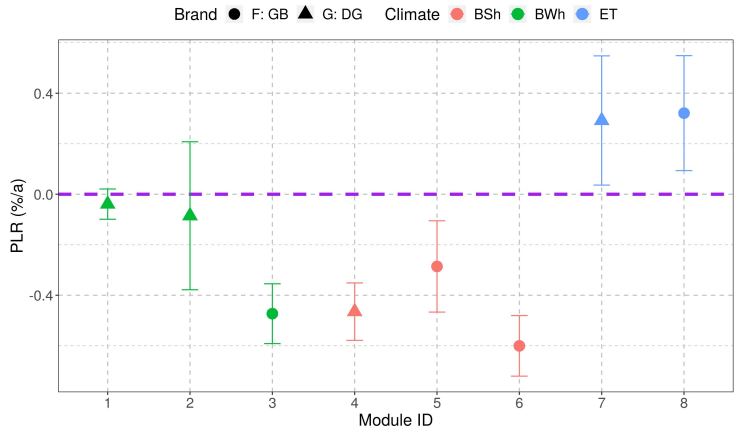

Figure 3: Median PLR and 83.4% confidence interval for all eight modules.

$$[Q_1 - \gamma(Q_3 - Q_1), Q_3 + \gamma(Q_3 - Q_1)] \tag{1}$$

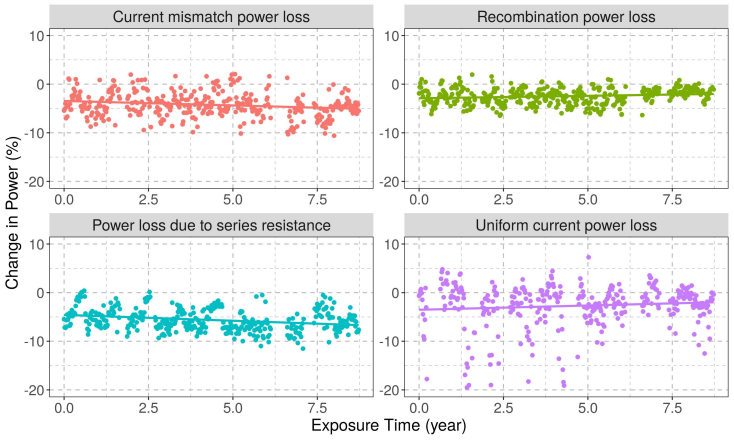

Figure 4: Normalized power loss factors obtained from outdoor I_{sc}-V_{oc} analysis for module 2 (BWh: DG).

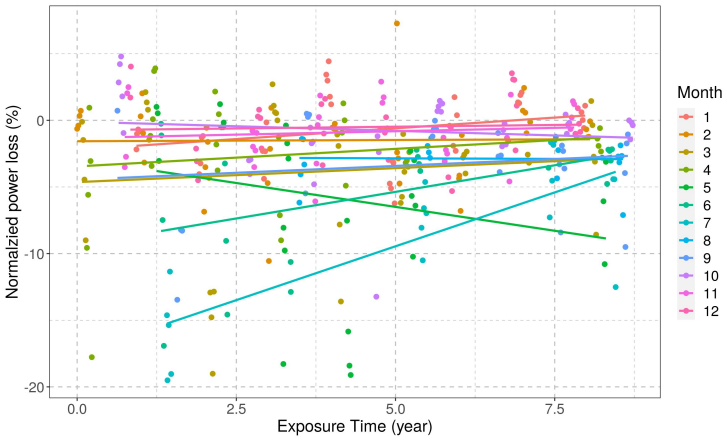

Figure 5: *Month-by-month* linear regression on the uniform current loss ($\Delta P_{I_{sc}}$) for module 2 (BWh: DG).

Next, the *month-by-month* regression is applied to the normalized power loss factors to get the rate of change of each loss factor for each module. Fig. 5 shows the result of uniform current loss (ΔP_{Isc}) of module 2 (BWh: DG) for each month through the 8.5+ year test period. We removed the linear slopes from months missing more than two years of observations or both the beginning and end years. For ΔP_{Isc} of module 2 (BWh: DG), the removed months are

July and August, and we use the remaining ten slopes to get the average and standard error to represent the rate of change.

Table 2: AVERAGE AND STANDARD ERROR OF THE RATE OF CHANGE IN EACH POWER LOSS MODE FOR EACH MODULE.

ID	Average (%/a)				Standard Error (%/a)			
	ΔP_{Isc}	ΔP_{Voc}	ΔP_{Rs}	ΔP_{Imis}	ΔP_{Isc}	ΔP_{Voc}	ΔP_{Rs}	ΔP_{Imis}
1	**-0.2234**	0.0045	-0.0360	-0.1840	0.0369	0.0362	0.0475	0.0902
2	0.1117	0.0908	**-0.2228**	-0.1438	0.1210	0.0318	0.0595	0.0566
3	**-0.8579**	-0.0474	0.0455	-0.0019	0.0911	0.0541	0.0604	0.1436
4	**-0.5908**	0.0310	-0.0350	0.0649	0.0729	0.0103	0.0426	0.0647
5	-1.2670	0.0892	-0.2205	0.7413	0.3678	0.0340	0.1516	0.2597
6	**-0.8503**	-0.0849	-0.0055	-0.0293	0.1075	0.0190	0.0532	0.1036
7	0.0239	0.1731	-0.2115	0.6246	0.7581	0.4819	0.3033	0.5406
8	-0.0366	0.0543	**-0.0766**	0.5776	0.3767	0.0366	0.0794	0.1447

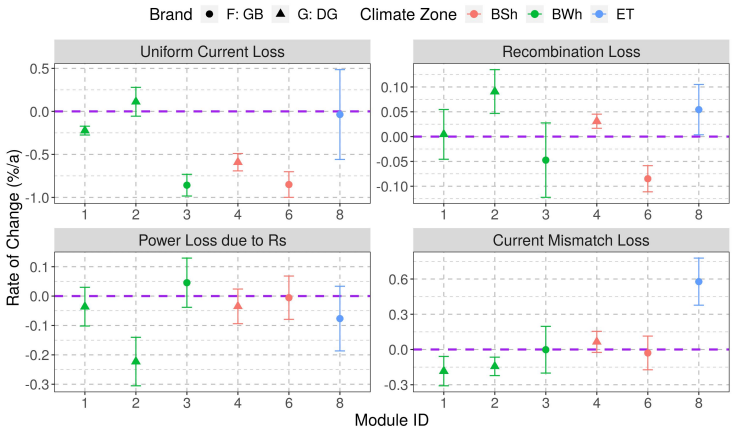

Figure 6: Average and 83.4% CI of the rate of change for each power loss mode from outdoor I_{sc}-V_{oc} analysis after removing modules 5 and 7.

Table 2 lists the average value and standard error of the rate of change of each power loss mode for all eight modules. Module 5 (BSh: GB) and module 7 (ET: DG) have relatively large standard errors due to the short system age (approximately three years), so we remove these two since our interest here is in long-term module degradation. Fig. 6 shows the 83.4% CI for the rate of change in each power loss mode.

4.2. Partial Shading Detection

The percentage of multistep I-V curves (MS (%)) for each module are listed in Table 3. The optimal hyperparameters for finding steps, k and m_{Δ}^{a}, were found to be 8 and 0.018, respectively, as trained on the whole dataset (all modules). Module 3 (BWh: GB), module 5 (BSh: GB), and module 6 (BSh: GB) have MS higher than the criterion (20% decided by the training dataset) and are therefore identified to experience partial shading. Module 3 (BWh: GB) is used here to illustrate the details in each part of partial shading results.

Table 3: The percentage of multistep I-V curves (MS) for all eight modules.

ID	System Age (Year)	Climate Zone	Brand	MS (%)
1	8.03	BWh	G:DG	2.97
2	8.74	BWh	G:DG	4.44
3	6.16	BWh	F:GB	**36.38**
4	6.39	BSh	G:DG	5.42
5	2.93	BSh	F:GB	**50.31**
6	6.39	BSh	F:GB	**50.65**
7	2.63	ET	G:DG	4.55
8	4.80	ET	F:GB	14.55

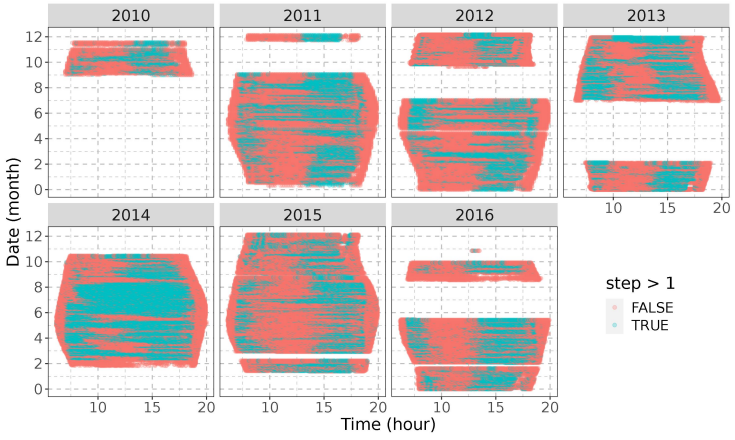

Figure 7: A partial shading diagram which visualizes the occurrence of multistep I-V curves for module 3 (BWh: GB).

Table 4: The shading profile of module 3 (BWh: GB): percentage of multistep I-V curves (MS) for peak partial shading times for each year.

Time in a Day	MS (%)	Year
08:10:00	35.1	2011
15:30:00	65.1	2011
07:10:00	46.9	2012
14:46:00	57.1	2012
08:10:00	55.7	2013
15:20:00	61.9	2013
08:40:00	58.9	2014
15:45:00	78.0	2014
07:55:00	32.1	2015
16:10:00	52.1	2015
07:50:00	40.0	2016
15:15:00	64.0	2016

A partial shading diagram (Fig. 7) visualizes the occurrence of multistep I-V curves in each year using time of day on the x-axis and date on the y-axis. The red points are for single step I-V curves and green points are for multistep I-V curves. The plotted points have transparency, so the color intensity correlates to the density of observations. The gaps along the y-axis indicate when the I-V tracer was offline and the pear-shaped border is due to the irradiance cutoff (5 $\mathrm{W/m^2}$) applied to remove the nighttime data. Table 4 shows the shading profile of module 3 (BWh: GB) for each year, which quantifies when partial shading occurred most frequently.

By converting the date and time of multistep I-V curves into the solar elevation and azimuth angles, using the longitude and latitude of the module's location, we can plot a shading Poynting vector diagram that shows the occurrence of multistep I-V curves (Fig. 8). The shading Poynting vector is so called because the colinearity of the relative solar position vector with the energy flux originating from the sun. Since both the PV module and the shading obstacle are stationary, the two angles corresponding to clusters of multistep (green) points indicate the relative position of the obstacles that cast shadows on the PV module. We find the localized MS peak location in the solar azimuth angle

to locate shading obstacles, as listed in Table 5.

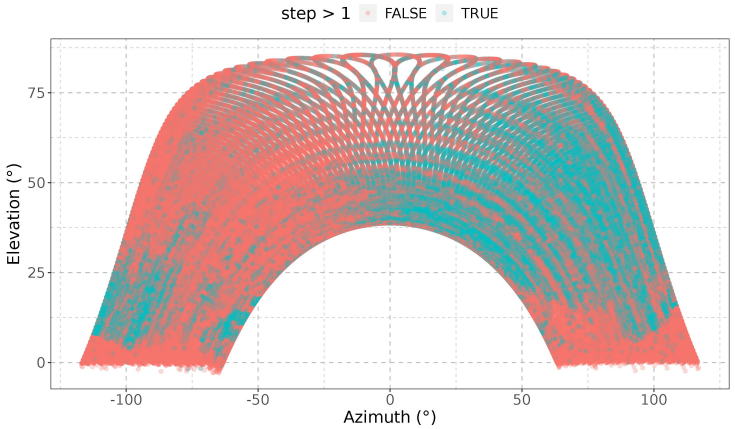

Figure 8: A shading Poynting vector diagram showing the occurrence of multistep I-V curves for module 3 (BWh: GB) with solar position angles as coordinates. The shading Poynting vector is collinear with the flux originating from the sun.

Table 5: Solar azimuth angle with peak MS for all three PV modules identified to have partial shading problems.

Module ID	Solar azimuth angle (°)	MS (%)
3	-99	34.9
	35	53.5
	87	52.7
5	-84	60.1
	-11	72.7
6	-88	67.4
	-34	71.6
	81	42.3

Fig. 9 shows the distribution of I-V curve middle step locations in voltage for multistep I-V curves. We can now extract the start and end voltages of each local peak. For module 3 (BWh: GB), the first peak is close to 0 and exhibits quite low density; this is not a real steps' location existing in the I-V curves,

but arises due to the spline model used in *ddiv* and the fluctuation of datapoints close to the I_{sc} region of the curve. Additionally, there are too few datapoints in such a narrow voltage range to determine the existence of a step at this low voltage. We use the start and end voltages of the remaining multistep peaks in Fig. 9 to classify each multistep I-V curve into one of the three shading scenarios described in the methods section, with the results summarized in Table 6.

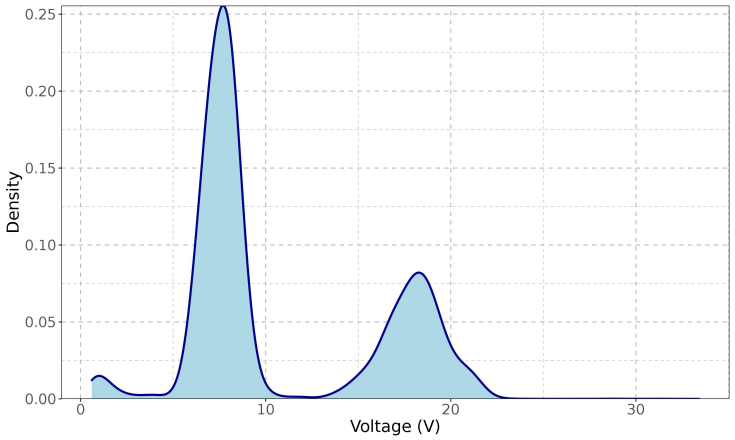

Figure 9: The density of voltage locations for the middle I-V steps for modules 3 (the I-V steps except V_{oc}, approximately 34 Volts).

Table 6: Classification of shading scenarios based on voltage clusters of I-V steps' location. Case 1: One bypass diode activated; Case 2: Two bypass diodes activated with same current mismatch; Case 3: Two bypass diodes activated with different current mismatch.

Module ID	Case 1 (%)	Case 2 (%)	Case 3 (%)
3	22.86	61.19	15.95
5	26.54	59.93	13.52
6	25.19	36.67	38.13

The classification of persistent and transient multistep I-V curves is based on the existence of a multistep I-V curve "neighbor" in the time-series data, such that the multistep curve persists through time, as opposed to being transient and

only seen once in between single step I-V curves. The percentage of persistent multistep I-V curves are 89.9%, 92.0%, and 95.2% for module 3 (BWh: GB), module 5 (BSh: GB) and module 6 (BSh: GB), respectively. Fig. 10 shows the distribution of the duration of persistent multistep I-V curves for module 3 (BWh: GB), the peak is 12 minutes. The peak of module 5 (BSh: GB) and module 6 (BSh: GB) are located at 11 and 12 minutes, respectively.

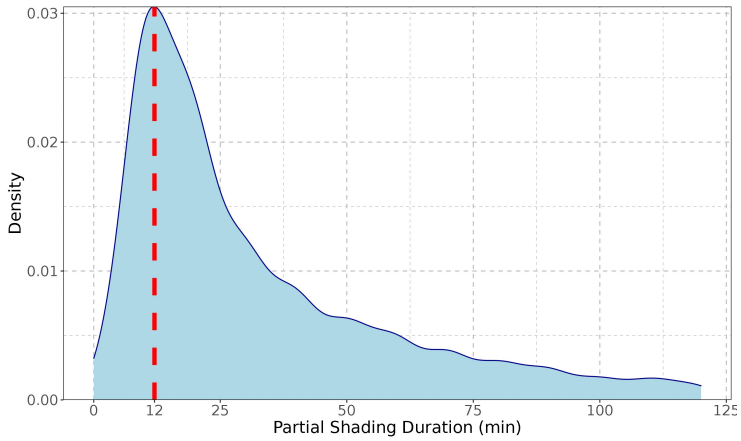

Figure 10: Distribution of the duration of persistent multistep I-V curves for module 3 (BWh: GB).

5. Discussion

From simple time-series datastreams of P_{mp} and I-V curves acquired from single PV modules, we have demonstrated the determination of module performance loss, active degradation modes, and patterns and characteristics of module partial shading. The techniques we employ can also be adapted and applied to strings of modules. Therefore these relatively simple datastreams can provide a PV power plant owner, or operations and maintenance provider, the information needed to diagnose and remediate their systems on an ongoing basis.

5.1. Long-term Performance Loss and Module Degradation Mechanisms

From the PLR result shown in Fig. 3, BSh causes faster degradation than BWh considering all the PV modules studied, and this is especially true for the double-glass PV modules. At a 5% statistical significance level (95% confidence), the average PLR of module 1 (BWh: DG) is more positive (exhibits less degradation) than that of module 4 (BSh: DG). The climate ET is the mildest climate zone studied here for inducing PV module degradation, and both modules there exhibit PLR values that are not significantly different from zero. This finding is further supported by null hypothesis significance testing (Kulinskaya et al. (2011); van Dongen et al. (2019)), whereby the 95% CI for module 7 (ET: DG) and module 8 (ET: GB) are 0.6542%/a ± -0.0699%/a and 0.6434%/a ± -0.0010%/a, respectively. Both of these CI ranges include 0, confirming the null hypothesis, and demonstrating that these modules effectively did not degrade over their studied system ages. Double-glass modules, brand G, show better performance than glass-backsheet modules (brand F) in the BWh climate zone. Performance of the two brands is more comparable in BSh and ET climate zones.

Table 2 shows the dominant power loss mode (in bold text) for the six modules with system ages longer than three years; the dominant power loss modes have the most negative rate of change. The dominant power loss mode for the five modules included in Fig. 6, located in BWh and BSh climates, is the uniform current loss, except for module 2 (BWh: DG). Module 2 (BWh: DG) is less comparable to the other DG modules; though fabricated by the same company, it is a different model and vintage, and the number of cells and bypass diodes are different from other double-glass modules as recorded in Table 1. Comparing the rate of change of the four power loss modes for module 1 (BWh: DG) and module 4 (BSh: DG), the maximal difference (0.3678%) occurs for the dominant power loss mode, ΔP_{Isc}, with a 5% significance level, as shown in Fig. 6. The BWh climate zone caused significantly less change in ΔP_{Isc} compared to the BSh climate zone for double-glass modules. But for glass-backsheet modules, comparing module 3 (BWh: GB) and module 6 (BSh: GB),

the rate of the four power loss modes are very similar and the maximal difference is less than 0.05%. This finding supports the PLR results, which find that the double-glass modules are more different between BWh and BSh climate zones than glass-polymeric backsheet modules. The outdoor I_{sc}-V_{oc} and loss factor method helps to further identify that this performance difference is primarily due to the increased uniform current power loss for the BSh-fielded double-glass modules. The dominant power loss mode for glass-backsheet modules located in ET is ΔP_{Rs}, but the average is not significantly different from zero, as can be inferred from Fig. 6.

5.2. Partial Shading and the Local Environment

In this study, modules 3 (BWh: GB), 5 (BSh: GB), and 6 (BSh: GB) are found to experience frequent partial shading. All three of the PV modules have MS significantly higher than the detection accuracy criterion of 20%, and these values are also significantly higher than any of the other modules as summarized in Table 3. These PV modules are all brand F modules with glass-polymeric backsheet architecture, but we believe the module architecture is unrelated to the partial shading observed; the bypass diodes installed in all commercial PV modules are supposed to activate when the PV module experiences partial shading. The difference in MS between these three modules and the others is most likely due to differences in the local surroundings, of their specific installation locations.

The partial shading diagram shown in Fig. 7 is a very useful data visualization showing temporal patterns of partial shading. However for system diagnosis, quantitative results are preferred, so we developed the shading profile as summarized in Table 4. Here we chose an annual reporting period for the shading profile. One can shorten this time period to allow more frequent monitoring, as long as the number of I-V curves is sufficient for finding the localized peaks of MS. Consistent times of day when shading occurs is found, for example, in the shading profile of module 3 (BWh: GB): there is one peak in the morning located around 8 am and another peak in the afternoon near

3:30 pm.

The shading Poynting vector diagram, shown in Fig. 8, is more helpful to locate shading obstacles on a map if on-site inspection is unavailable. The solar azimuth angle corresponding to the local peak of the MS is summarized from Fig. 8 in Table 5, providing detailed insights for shading remediation. The empty space at high solar elevation angle in Fig. 8 is caused by the five minute time interval of the data, which has a relatively low resolution at noon due to the faster change in solar azimuth angle with time during these months (summer in the northern hemisphere). The solar azimuth angle reported in Table 5 that is close to 0 ° corresponds to the obstacle that is most important to remove since it is right in front of the module under study, and obscures the module during the highest insolation period of the day. While this analysis can be applied using different time periods to allow more frequent monitoring similar to the shading profile, the results presented here use the complete system age.

As for the shading scenarios (1 vs 2 bypass diodes activated, similar vs dissimilar current mismatch for 2 bypass diodes), module 3 (BWh: GB) and module 5 (BSh: GB) have similar percentages in each case as recorded in Table 6. The dominant case for both of those modules corresponds to two bypass diodes being activated with similar current mismatches. Meanwhile for module 6 (BWh: GB), the percentage of each case is quite comparable. In addition, the percentage of persistent multistep I-V curves is in the range of 89.9% to 95.3%, which indicates that the five minute time interval of the I-V datastreams are long enough to capture most of the continuity in partial shading. The distribution of the duration of persistent multistep I-V curves, shown in Fig. 10 for module 3, are all right-skewed with a peak located around 11 to 12 minutes. This approximate 10 minute duration of partial shading is relatively short (2 consecutive I-V measurements) considering that a stable object would continuously cast shadows on the module. We believe this could be caused by unstable weather conditions, and/or occasional I-V curve misclassification by the step detection algorithm such that a long duration of partial shading is broken up into several shorter periods.

The partial shading detection method, based on time-series multistep I-V curves, has the advantage of not requiring a reference system for comparison. However, partial shading does not always activate bypass diodes and thereby cause multiple steps in I-V curves. If the bypass diode is broken or if the partial shading situation is the same for all cell strings in the module (e.g., for inter-row shading of portrait-oriented modules), such cases won't be captured by this approach.

Partial shading is a known risk factor for module degradation. The effects of frequent partial shading are well known for fixed shading objects located very close to an array and shade the same area of a module and block a large percentage of the incident light, repeatedly and for long periods of time. The resulting repetitive and persistent hot spotting and activation of the same bypass diode can lead to materials changes in the module, and eventual failure of the bypass diode. Long-term, close-range partial shading can even lead to safety issues such as electrical shorts or fires.

Close-range shading obstacles are easily identified in the field, particularly for a research system such as the one studied here. Furthermore, close-range partial shading would influence ΔP_{Imis} (power loss related to current mismatch), due to persistent unequal shading and degradation of different cell strings. ΔP_{Imis} accounts for changes in mismatch due to both 1) evolving string-level performance differences within a module, and 2) changes in the shading profile of the module. ΔP_{Imis} does not significantly worsen for any of the modules that were detected to experience frequent partial shading, so this agrees with the module operator's assessment that none of the shading obstacles detected in our Poynting vector or shading profile analyses are close to the modules.

The I_{sc}-V_{oc} loss factor results for the modules that experience a high percentage of multistep I-V curves may however suggest that frequent partial shading from distant objects can contribute to module degradation. Distant objects cause a smaller degree of current mismatch, as the amount of diffuse light reaching the shaded string is greater than for shading caused by nearby objects. Shading patterns from distant objects are also likely to traverse the

surface of the module, and therefore cause more comparable shading of each cell string throughout the course of a day. Modules 3, 5, and 6, which experienced the greatest percentages of partial shading (above concluded to be due to distant objects), also showed the greatest uniform current loss power degradation (ΔP_{Isc}) of all modules studied. Modules 3 and 6 are included in our long-term degradation study, and degraded similarly as shown in PLR (Fig. 3) and power loss factor results Fig. 6. While these modules happened to be of a single brand, the fact that they both experienced relatively high frequency partial shading could contribute this similarity in degradation.

6. Conclusions

In this research, we obtain the PLR and four power loss mode rates of change that relate to the active degradation mechanisms of eight modules installed in the field for up to nine years. Methods to analyze time-series P_{mp} and I-V curves included the XbX + UTC predictive method with *year-on-year* regression, and outdoor I_{sc}-V_{oc} and loss factor calculation. The results show that the BSh Köppen-Geiger climate zone causes faster degradation considering both brands/architectures of PV modules under study, while the ET climate zone causes the slowest degradation. The dominant degradation mode for most modules located in BWh and BSh is uniform current power loss. Double-glass modules (the same model) have better performance in the BWh climate zone compared to BSh climate zone, mainly due to a reduction in the rate of change in uniform current loss. Glass-polymer backsheet modules located in BWh and BSh climate zones have similar rates of change for each power loss mode. The study procedure and methods we used for the long-term degradation study can be generalized to a larger population of PV modules and systems, including strings of modules. We presented a statistical partial shading detection method based on time-series I-V curve datastreams, which is able to return the temporal shading profile, the shading Poynting vector representing the relative locations of shading obstacles, classification of shading scenarios, and the distribution of

partial shading duration. The result shows three of the modules in the dataset experience frequent partial shading. The five minute time interval of the I-V datastreams is sufficient to capture over 90% continuity of the partial shading occurrences on average. The degradation mechanism study, using outdoor I_{sc}-V_{oc}, and the partial shading study share common initial processing steps, which can reduces the analysis effort required for quantifying partial shading. Frequent and persistent partial shading is a potential local environmental stressor, which should be considered in degradation studies. This partial shading detection method is unable to capture the particular partial shading case where the same shadow is uniformly present on each cell string in a module or array. At the same time, this method realizes partial shading detection using only data from the studied module or system, without requiring a separate reference system for comparison. Partial shading detection using time-series I-V curves provides a quantitative method to bridge the gap between I-V curve shape and specific shading scenarios for PV modules in the field.

7. Acknowledgment

This material is based upon work supported by the U.S. Department of Energys Office of Energy Efficiency and Renewable Energy (EERE) under Solar Energy Technologies Office (SETO) Agreement Number DE-EE-0008550. The views expressed herein do not necessarily represent the views of the U.S. Department of Energy or the United States Government. This work made use of the High Performance Computing Resource in the Core Facility for Advanced Research Computing at Case Western Reserve University. Sandia National Laboratories is a multimission laboratory managed and operated by National Technology & Engineering Solutions of Sandia, LLC, a wholly owned subsidiary of Honeywell International Inc., for the U.S. Department of Energys National Nuclear Security Administration under contract DE-NA0003525.

References

Basri, Y. e., Bressan, M., Sguier, L., Alawadhi, H. A., & Alonso, C. (2015). A proposed graphical electrical signatures supervision method to study PV module failures. *Solar Energy*, . doi:https://doi.org/10.1016/j.solener.2015.02.048.

Borchers, H. W. (2019). pracma: Practical Numerical Math Functions. URL: https://CRAN.R-project.org/package=pracma.

Bryant, C., Wheeler, N. R., Rubel, F., & French, R. H. (2017). Kgc: Koeppen-Geiger Climatic Zones. URL: https://CRAN.R-project.org/package=kgc.

Cozzi, L., Gould, T., & Birol, F. (2020). *World Energy Outlook 2020*. Paris, France: IEA. URL: https://www.iea.org/reports/world-energy-outlook-2020.

Cumming, G., & Finch, S. (2005). Inference by eye: Confidence intervals and how to read pictures of data. *American Psychologist*, (pp. 170–180). doi:10.1037/0003-066X.60.2.170.

Curran, A., Burleyson, T., Lindig, S., Moser, D., & French, R. (2020). PVplr: Performance Loss Rate Analysis Pipeline. URL: https://CRAN.R-project.org/package=PVplr.

Curran, A. J., Birk Jones, C., Lindig, S., Stein, J., Moser, D., & French, R. H. (2019). Performance Loss Rate Consistency and Uncertainty Across Multiple Methods and Filtering Criteria. In *2019 IEEE 46th Photovoltaic Specialists Conference (PVSC)* (pp. 1328–1334). doi:10.1109/PVSC40753.2019.8980928 iSSN: 0160-8371.

Davis, K. O., Kurtz, S. R., Jordan, D. C., Wohlgemuth, J. H., & Sorloaica-Hickman, N. (2013). Multi-pronged analysis of degradation rates of photovoltaic modules and arrays deployed in Florida. *Progress in Photovoltaics: Research and Applications*, *21*, 702–712. doi:10.1002/pip.2154.

van Dongen, N. N. N., van Doorn, J. B., Gronau, Q. F., van Ravenzwaaij, D., Hoekstra, R., Haucke, M. N., Lakens, D., Hennig, C., Morey, R. D., Homer, S., Gelman, A., Sprenger, J., & Wagenmakers, E.-J. (2019). Multiple Perspectives on Inference for Two Simple Statistical Scenarios. *The American Statistician*, *73*, 328–339. doi:10.1080/00031305.2019.1565553.

ET Instrumente GmbH (). *ESL Solar 500 Made by ET Instrumente GmbH*. Technical Report ET Instrumente GmbH Neckarauer Str. 2 68766 Hockenheim.

Firth, K. S., Lomas, K., & Simon, R. (2009). A simple model of PV system performance and its use in fault detection. *Solar Energy*, . doi:https://doi.org/10.1016/j.solener.2009.08.004.

French, R. H., Bruckman, L. S., Moser, D., Lindig, S., van Iseghem, M., Müller, B., Stein, J. S., Richter, M., Herz, M., Sark, W. V., Baumgartner, F., Ascencio-Vásquez, J., Bertani, D., Maugeri, G., Curran, A. J., Rath, K., Liu, J., Khalilnejad, A., Meftah, M., Jordan, D., Deline, C., Makrides, G., Georghiou, G., Livera, A., Meyers, B., Plessis, G., Theristis, M., & Luo, W. (2021). Assessment of Performance Loss Rate of PV Power Systems. In *Assessment of Performance Loss Rate of PV Power Systems* number T13-22:2021 in IEA-PVPS. IEA-PVPS. URL: https://iea-pvps.org/key-topics/assessment-of-performance-loss-rate-of-pv-power-systems/.

French, R. H., Podgornik, R., Peshek, T. J., Bruckman, L. S., Xu, Y., Wheeler, N. R., Gok, A., Hu, Y., Hossain, M. A., Gordon, D. A., Zhao, P., Sun, J., & Zhang, G. (2015). Degradation science: Mesoscopic evolution and temporal analytics of photovoltaic energy materials. *Current Opinion in Solid State and Materials Science*, *19*, 212–226. doi:10.1016/j.cossms.2014.12.008.

Gok, A., Ozkalay, E., Friesen, G., & Frontini, F. (2021). Power Loss Modes of Building-Integrated Photovoltaic Modules: An Analytical Approach Using

Outdoor $I-V$ Curves. *IEEE Journal of Photovoltaics*, (pp. 1–8). doi:10.1109/JPHOTOV.2021.3060719.

Gow, J. A., & Manning, C. D. (1999). Development of a photovoltaic array model for use in power-electronics simulation studies. *IEE Proceedings - Electric Power Applications*, *146*, 193–200. URL: https://digital-library.theiet.org/content/journals/10.1049/ip-epa_19990116. doi:10.1049/ip-epa:19990116. Publisher: IET Digital Library.

Hasselbrink, E., Anderson, M., Defreitas, Z., Mikofski, M., Shen, Y.-C., Caldwell, S., Terao, A., Kavulak, D., Campeau, Z., & DeGraaff, D. (2013). Validation of the PVLife model using 3 million module-years of live site data. In *IEEE 39th Photovoltaic Specialists Conference (PVSC)* (pp. 0007–0012). IEEE. URL: http://ieeexplore.ieee.org/xpls/abs_all.jsp?arnumber=6744087. doi:10.1109/PVSC.2013.6744087.

Hemza, A., Abdeslam, H., Rachid, C., & Aoun, N. (2019). Simplified methods for evaluating the degradation of photovoltaic module and modeling considering partial shading. *Measurement*, *138*, 217–224. URL: http://www.sciencedirect.com/science/article/pii/S0263224119301071. doi:10.1016/j.measurement.2019.01.098.

Huang, W.-H., Xuan Ma, Jiqi Liu, Menghong Wang, Alan J. Curran, Fada, J. S., Jean-Nicolas Jaubert, Jing Sun, Jennifer L. Braid, Jenny Brynjarsdottir, & Roger H. French (2021). Ddiv: Data Driven I-v Feature Extraction. Comprehensive R Archive Network (CRAN). URL: https://CRAN.R-project.org/package=ddiv.

Jones, C. B., Hamzavy, B., Hobbs, W. B., Libby, C., & Lavrova, O. (2018). IEC 61215 Qualification Tests vs Outdoor Performance using Module Level In Situ I-V Curve Tracing Devices. In *2018 IEEE 7th World Conference on Photovoltaic Energy Conversion (WCPEC) (A Joint Conference of 45th IEEE PVSC, 28th PVSEC 34th EU PVSEC)* (pp. 1286–1291). doi:10.1109/PVSC.2018.8548222.

Jones, C. B., & Hansen, C. W. (2019). Single Diode Parameter Extraction from In-Field Photovoltaic I-V Curves on a Single Board Computer. In *2019 IEEE 46th Photovoltaic Specialists Conference (PVSC)* (pp. 0382–0387). doi:10.1109/PVSC40753.2019.8981330.

Jordan, D., & Kurtz, S. (2010). Analytical improvements in PV degradation rate determination. In *2010 35th IEEE Photovoltaic Specialists Conference* (pp. 002688–002693). doi:10.1109/PVSC.2010.5617074 iSSN: 0160-8371.

Jordan, D., Smith, R., Osterwald, C., Gelak, E., & Kurtz, S. (2010). Outdoor PV degradation comparison. In *2010 35th IEEE Photovoltaic Specialists Conference* (pp. 002694–002697). Honolulu, HI, USA: IEEE. URL: http://ieeexplore.ieee.org/document/5616925/. doi:10.1109/PVSC.2010.5616925.

Jordan, D. C., Deline, C., Kurtz, S. R., Kimball, G. M., & Anderson, M. (2018). Robust PV Degradation Methodology and Application. *IEEE Journal of Photovoltaics*, *8*, 525–531. doi:10.1109/JPHOTOV.2017.2779779. Conference Name: IEEE Journal of Photovoltaics.

Killam, A. C., Karas, J. F., Augusto, A., & Bowden, S. G. (2021). Monitoring of Photovoltaic System Performance Using Outdoor Suns-VOC. *Joule*, *5*, 210–227. doi:10.1016/j.joule.2020.11.007.

Kratochvil, J. A., Boyson, W. E., & King, D. L. (2004). *Photovoltaic array performance model.*. Technical Report SAND2004-3535 Sandia National Laboratories. URL: https://www.osti.gov/biblio/919131-photovoltaic-array-performance-model. doi:10.2172/919131.

Kulinskaya, E., Morgenthaler, S., & Staudte, R. G. (2011). Significance Testing: An Overview. In M. Lovric (Ed.), *International Encyclopedia of Statistical Science* (pp. 1318–1321). Berlin, Heidelberg: Springer. doi:10.1007/978-3-642-04898-2_514.

Lindig, S., Kaaya, I., Weiss, K.-A., Moser, D., & Topic, M. (2018). Review of Statistical and Analytical Degradation Models for Photovoltaic Modules and Systems as Well as Related Improvements. *IEEE Journal of Photovoltaics*, *8*, 1773–1786. doi:10.1109/JPHOTOV.2018.2870532. Conference Name: IEEE Journal of Photovoltaics.

Lindig, S., Moser, D., Curran, A. J., Rath, K., Khalilnejad, A., French, R. H., Herz, M., Müller, B., Makrides, G., Georghiou, G., Livera, A., Richter, M., Ascencio-Vásquez, J., van Iseghem, M., Meftah, M., Jordan, D., Deline, C., van Sark, W., Stein, J. S., Theristis, M., Meyers, B., Baumgartner, F., & Luo, W. (2021). International collaboration framework for the calculation of performance loss rates: Data quality, benchmarks, and trends (towards a uniform methodology). *Progress in Photovoltaics: Research and Applications*, *29,6*. doi:10.1002/pip.3397.

Liu, J., Wang, M., Curran, A. J., Maroof Karimi, A., Huang, W.-h., Schnabel, E., Khl, M., Braid, J. L., & French, R. H. (2019). Real-world PV Module Degradation across Climate Zones Determined from Suns-Voc, Loss Factors and I-V Steps Analysis of Eight Years of I-V, Pmp Time-series Datastreams. In *2019 IEEE 46th Photovoltaic Specialists Conference (PVSC)* (pp. 0680–0686). doi:10.1109/PVSC40753.2019.8980541 iSSN: 0160-8371.

Marion, B., Adelstein, J., Boyle, K., Hayden, H., Hammond, B., Fletcher, T., Canada, B., Narang, D., Kimber, A., Mitchell, L., Rich, G., & Townsend, T. (2005). Performance parameters for grid-connected PV systems. In *Conference Record of the Thirty-First IEEE Photovoltaic Specialists Conference, 2005.* (pp. 1601–1606). doi:10.1109/PVSC.2005.1488451.

Meyers, B., & Mikofski, M. (2017). Accurate Modeling of Partially Shaded PV Arrays. In *2017 IEEE 44th Photovoltaic Specialist Conference (PVSC)* (pp. 3354–3359). doi:10.1109/PVSC.2017.8521559.

Nehme, B., Msirdi, N. K., Namaane, A., & Akiki, T. (2017). Analysis and Characterization of Faults in PV Panels. *Energy Procedia*, *111*,

1020–1029. URL: http://www.sciencedirect.com/science/article/pii/S1876610217302989. doi:10.1016/j.egypro.2017.03.265. ZSCC: 0000014.

Perea, A., Smith, C., Davis, M., Mond, A., Gallagher, B., Shawn Rumery, Aaron Holm, Rachel Goldstein, & Justin Baca (2019). *U. S. Solar Market Insight Report 2018 Year In Review*. Technical Report Solar Energy Industries Association. URL: https://www.seia.org/research-resources/solar-market-insight-report-2018-year-review.

Peshek, T. J., Fada, J. S., Hu, Y., Xu, Y., Elsaeiti, M. A., Schnabel, E., Köhl, M., & French, R. H. (2016). Insights into metastability of photovoltaic materials at the mesoscale through massive I–V analytics. *Journal of Vacuum Science & Technology B*, *34*, 050801. doi:10.1116/1.4960628.

Phinikarides, A., Kindyni, N., Makrides, G., & Georghiou, G. E. (2014). Review of photovoltaic degradation rate methodologies. *Renewable and Sustainable Energy Reviews*, *40*, 143–152. URL: http://www.sciencedirect.com/science/article/pii/S1364032114006078. doi:10.1016/j.rser.2014.07.155.

Pordis (2018). Pordis, LLC - In-Line String-Level I-V Tracer. http://www.pordis.com/products.html.

R Core Team (2020). R: The R Project for Statistical Computing. URL: https://www.r-project.org/.

Rubel, F., Brugger, K., Haslinger, K., & Auer, I. (2017). The climate of the European Alps: Shift of very high resolution Kppen-Geiger climate zones 18002100. *Meteorologische Zeitschrift*, *26*, 115–125. URL: http://www.schweizerbart.de/papers/metz/detail/26/87237/The_climate_of_the_European_Alps_Shift_of_very_hig?af=crossref. doi:10.1127/metz/2016/0816.

Siyu Guo, Eric Schneller, Joe Walters, Kristopher O. Davis, & Winston V.

Schoenfeld (2016). Detecting loss mechanisms of c-Si PV modules in-situ I-V measurement. In *Proc.SPIE*. volume 9938. doi:10.1117/12.2236939.

Smith, R. M., Jordan, D. C., & Kurtz, S. R. (2012). *Outdoor PV Module Degradation of Current-Voltage Parameters: Preprint*. Technical Report NREL/CP-5200-53713 National Renewable Energy Lab. (NREL), Golden, CO (United States). URL: https://www.nrel.gov/docs/fy12osti/53713.pdf.

Teodorescu, R., Kerekes, T., Sera, D., & Spataru, S. (2015). Monitoring and Fault Detection in Photovoltaic Systems Based On Inverter Measured String I-V Curves. *31st European Photovoltaic Solar Energy Conference and Exhibition*, (pp. 1667–1674). URL: http://www.eupvsec-proceedings.com/proceedings?paper=35531. doi:10.4229/EUPVSEC20152015-5BO.12.2. ZSCC: 0000002 ISBN: 9783936338393 Publisher: WIP.

Thieurmel, B., & Elmarhraoui, A. (2019). Suncalc: Compute Sun Position, Sunlight Phases, Moon Position and Lunar Phase. URL: https://CRAN.R-project.org/package=suncalc.

Tsafarakis, O., Sinapis, K., & van Sark, W. G. J. H. M. (2019). A Time-Series Data Analysis Methodology for Effective Monitoring of Partially Shaded Photovoltaic Systems. *Energies*, *12*, 1722. URL: https://www.mdpi.com/1996-1073/12/9/1722. doi:10.3390/en12091722.

Tukey, J. (1977). *Exploratory Data Analysis*. (1st ed.). Reading, Mass. ISBN: 978-0-201-07616-5 Publisher: Pearson.

Wang, M., Liu, J., Burleyson, T. J., Schneller, E. J., Davis, K. O., French, R. H., & Braid, J. L. (2020). Analytic Isc-Voc Method and Power Loss Modes From Outdoor Time-Series I-V Curves. *IEEE Journal of Photovoltaics*, *10*, 1379–1388. doi:10.1109/JPHOTOV.2020.2993100. Conference Name: IEEE Journal of Photovoltaics.

Wang, M., Tyler J. Burleyson, Jiqi Liu, Alan J. Curran, Abdulkerim Gok, Eric J. Schneller, Kristopher O. Davis, Jennifer L. Braid, & Roger H. French (2021). SunsVoc: Constructing Suns-Voc from Outdoor Time-Series I-V Curves. Comprehensive R Archive Network (CRAN). URL: `https://CRAN.R-project.org/package=SunsVoc`.

Whitaker, C., Townsend, T., Newmiller, J., King, D., Boyson, W., Kratochvil, J., Collier, D., & Osborn, D. (1997). Application and validation of a new PV performance characterization method. In *Conference Record of the Twenty Sixth IEEE Photovoltaic Specialists Conference - 1997* (pp. 1253–1256). doi:`10.1109/PVSC.1997.654315`.